ARTICLE OPEN

Redefining passivity breakdown of super duplex stainless steel by electrochemical operando synchrotron near surface X-ray analyses

Marie Långberg (1), Cem Örnek (1), Jonas Evertsson^{3,4,5}, Gary S. Harlow³, Weronica Linpé³, Lisa Rullik (1), Francesco Carlà^{6,7}, Roberto Felici^{6,8}, Eleonora Bettini⁹, Ulf Kivisäkk (1), Edvin Lundgren (1) and Jinshan Pan (1)

Passivity determines corrosion resistance and stability of highly-alloyed stainless steels, and passivity breakdown is commonly believed to occur at a fixed potential due to formation and dissolution of Cr(VI) species. In this work, the study of a 25Cr–7Ni super duplex stainless steel in 1 M NaCl solution revealed that the passivity breakdown is a continuous degradation progress of the passive film over a potential range, associated with enhanced Fe dissolution before rapid Cr dissolution and removal of the oxide. The breakdown involves structural and compositional changes of the passive film and the underlying alloy surface layer, as well as selective metal dissolution depending on the anodic potential. The onset of passivity breakdown occurred at 1000 mV/ $_{Ag/AgCI}$, and Fe dissolved more on the ferrite than the austenite phase. With increasing potential, the passive film became thicker but less dense, while the underlying alloy surface layer became denser indicating Cr dissolution occurred at Cr dissolu

npj Materials Degradation (2019)3:22; https://doi.org/10.1038/s41529-019-0084-3

INTRODUCTION

Passivity has vital importance to our civilization because corrosion resistance of most of metallic materials used today is due to spontaneous formation of a passive film on the surface, preventing the materials from rapid degradation.^{1,2} The electrochemical characteristics of passivating metals are reflected by their current-potential behavior showing a transition from an active (high current) to passive (low current) state. The presence of the passive film decreases the corrosion rate by orders of magnitude.3-7 However, passivity breakdown can occur in corrosive environments, leading to a sharp increase of the anodic current at the so-called breakdown potential. When this happens, either the passive film breaks locally triggering localized corrosion, or it vanishes allowing rapid dissolution leading to material failure with serious consequences. 1-3,8-11 The passivity and breakdown behavior of metals have been studied extensively using electrochemical methods in corrosive aqueous electrolytes, often combined with surface analyses. There is ample literature regarding the thermodynamics, kinetics, and electrochemical characteristics of passivity.^{3–7,12–14} Most of early studies of passivity breakdown focused on pitting initiation related to nonmetallic inclusions (e.g., MnS) existing in stainless steels.¹⁵ This problem has been mitigated by reducing the S and Mn contents of the stainless steels. However, many advanced alloys nowadays contain multi-elements and consist of multi-phase microstructures, where different kinds of precipitates and phase/grain boundaries may trigger localized corrosion. 16-23 Further studies are necessary to better understand the passivity and its breakdown of such alloys.

The thickness, composition, and structure of the passive film, in particular of Fe-based and Ni-based alloys, have been investigated, ex situ, by X-ray photoelectron spectroscopy (XPS), Auger electron spectroscopy (AES), and secondary ion mass spectrometry, and sometimes also by transmission electron diffraction and X-ray scattering.^{24–26} Scanning tunneling microscopy (STM) and atomic force microscopy (AFM) have been used, both ex situ and in situ, to investigate the atomic structure, roughness, and topography of the outermost surface layers of various metals. 13,14,27-30 Recently, efforts have been made to investigate the effects of aging³¹ and heating at elevated temperatures on the passive film.^{32,33} Transpassive breakdown at high electrochemical potentials has also been investigated.^{34–38} The composition and structure of passive films formed under aqueous environments may get changed when the samples are analyzed under ultra-high vacuum (UHV) conditions; therefore, efforts have been made to analyze the passive films under in situ conditions. 13,14,39,40 Most of the literature reports have focused on pure metals or simple alloys, while limited reports can be found on advanced commercial alloys with complicated composition and structure, such as duplex stainless steels. 41-52 Synchrotron-based analysis techniques, especially X-ray absorption spectroscopy and X-ray diffraction (XRD), have been used to analyze surface oxides or passive films on different metals under electrochemical control. 53-55 The valence state of atoms and their coordination numbers have been studied by using X-ray absorption near-edge structure and extended X-ray

¹Department of Chemistry, Division of Surface and Corrosion Science, KTH Royal Institute of Technology, 100 44 Stockholm, Sweden; ²Swerim AB, 16407 Kista, Sweden; ³Division of Synchrotron Radiation Research, Lund University, 221 00 Lund, Sweden; ⁴Deutsches Elektronen-Synchrotron (DESY), 22607 Hamburg, Germany; ⁵Physical Chemistry Department, Justus-Liebig-University Giessen, 35392 Giessen, Germany; ⁶Experimental Division, European Synchrotron Radiation Facility (ESRF), 38000 Grenoble, France; ⁷Diamond Light Source Ltd, Didcot, UK; ⁸SPINCNR, 00133 Roma, Italy and ⁹AB Sandvik Materials Technology, 811 81 Sandviken, Sweden Correspondence: Jinshan Pan (jinshanp@kth.se)

Received: 6 December 2018 Accepted: 8 May 2019

Published online: 28 May 2019



absorption fine structure analysis, but these were often limited to pure metals and binary alloys. ^{56–69} Synchrotron XRD measurements have been performed at grazing incidence (GIXRD) to analyze thin-surface layers with high resolution and sensitivity, showing advantages for rapid and detailed structural characterization. ^{70–75} Moreover, X-ray reflectivity (XRR) measurements have also been employed to study electrochemical oxide growth on pure metal and alloys. ^{76–80}

On the other hand, point defect model (PMD) has been developed to describe theoretically the generation and annihilation of ionic defects and the ionic flux via cationic/anionic vacancies in the oxide to define environmental and electrochemical conditions for growing, stable, and dissolving oxide films. 1,2,8,10,81,82 According to PDM, passivity is a dynamic process in which oxide formation and dissolution occur simultaneously. The passive state is a steady condition of a metal with a low dissolution rate, and passivity breakdown occurs when the oxide dissolution is faster than its formation. A pitting model was also reported being able to describe passivity breakdown including the role of the oxide layer. Moreover, efforts have been made to establish a "generalized model" to enable the description of the growth of oxide films on alloys under non-steady-state conditions.83 However, these theoretical models have been established mostly based on experiments conducted on pure metals and simple alloy systems, and further development is needed to describe passivity of multi-element/phase alloys. 82 A recent report has summarized various advancements in corrosion science via both experimental and theoretical approaches, and presented the current understanding of the mechanisms of corrosion initiation at atomic scale, including metal-water interfacial processes, surface atomic structure and reconstruction, hydroxylation, hydroxide and oxide formation, anodic and selective dissolution, effect of grain boundaries on passivity breakdown, etc.

In general, the passive films formed on highly alloyed stainless steels are 1–3 nm thick depending on the passivation conditions and consist mainly of Cr-oxides and Fe-oxides/hydroxides. Usually, Fe is enriched in the outer part and Cr is enriched in the inner part, and a small amount of Mo species (Mo⁴⁺, Mo⁶⁺) can also be present in the passive film.^{3–7,13,14} It was also reported that beneath the passive film there is an alloy surface layer that is enriched in Ni.^{3,14} The superior corrosion resistance of stainless steels has been ascribed to the Cr-rich surface oxide with Cr³⁺ state. The effective protection is lost when Cr³⁺ in the passive film is oxidized to higher oxidation states forming soluble Cr⁶⁺ species, so the oxide dissolution rate exceeds the formation rate, i.e., transpassive breakdown. ^{1,2,8,10,81,82} This appears as a drastic increase in the anodic current density by orders of magnitude, and without a stable protective oxide film on the surface, the stainless steel corrodes actively. ^{1–3,8–11,14,34–38}

The process of passivity breakdown of the advanced alloys, especially the transition from passive to transpassive state, has remained the least understood. 11 The challenge is to perform in situ and real-time analysis of the breakdown process of the passive film to elucidate the physiochemical and electrochemical reactions occurring at the interfaces as well as transport of ionic species across the thin oxide and hydroxide films. For the safe use and further development of high-performance alloys, it is of utmost importance to gain fundamental insight into passivity and its breakdown of highly corrosion-resistant alloys. This paper presents a multi-analytical study of the transpassive breakdown of 25Cr-7Ni super duplex stainless steel in 1 M NaCl solution using in situ and operando synchrotron XRR, XRF, and XRD measurements, in combination with electrochemical measurements including current transients and electrochemical impedance spectroscopy (EIS). The aim was to gain a comprehensive understanding of the mechanism and thus unravel the transpassive breakdown of this advanced alloy in chloride solution.

RESULTS

Current transients and EIS at applied potentials

The open-circuit potential of the sample in the solution was 125 mV/_{Aa/AaCl}. Figure 1 displays the anodic current density vs. time data recorded at applied potentials. At potentials below $1000\,\text{mV/}_{\text{Ag/AgCl}}$, the current density dropped quickly with time and reached a low level of $\sim 10^{-6}\,\text{A/cm}^{-2}$, typical for a passive state. At 1000 mV/Ag/AgCl, the current density initially decreased for <10 s, then increased slowly with time, indicating the onset of passivity breakdown. At 1100 mV/Ag/AgCI, the current density increased steadily with time to a high level, implying an enhanced anodic activity. Further increase of the potential resulted in a continuous increase of the current density to higher levels. Potentiodynamic polarization curves measured with a potential sweep rate of 10 mV/min also showed a drastic increase of the current density at $1000\,\text{mV/}_{\text{Ag/AgCI}}$ (Fig. S1 in Supplement Material). Apparently, the transition from passive to transpassive state started to occur at 1000 mV/Ag/AgCl as judged from the increasing anodic current. However, oxygen evolution reaction, occurring on the surface, may have also contributed to the high anodic current, especially at higher potentials.

Figure 2 displays Nyquist plots of the EIS spectra obtained at (a) open-circuit potential (OCP) and 900 mV/_{Ag/AgCl}, (b) 1000, and (c) 1100, 1200, and 1300 mV/_{Ag/AgCl}, respectively. At OCP and 900 mV, the EIS spectra exhibited one time-constant feature, appearing as a part of a large semicircle (Fig. 2a) with a high impedance level at low frequencies, typical for a passive state. In contrast, at 1000 mV, the spectrum showed a smaller semicircle and an inductive-like response at low frequencies (Fig. 2b). At higher applied potentials, the semicircle was further reduced and an inductive loop was seen at low frequencies (Fig. 2c), implying transpassive dissolution (or localized corrosion) occurring on the metal surface.³⁴ Clearly, a drastic change of the electrochemical characteristics of the sample surface occurred at 1000 mV/_{Ag/AgCl}, which indicates the onset of passivity breakdown, in agreement with the current transients.

Focusing on the main feature of the impedance response at different applied potentials, quantitative analysis of the EIS spectra could be done by spectra fitting using simple and plausible equivalent circuits as shown in the Supplement Material (Figs S2, S3). From the spectra fitting, the values of the charge transfer resistance and a constant phase element describing the capacitive response of the electrode-electrolyte interface were obtained (Table S1 in the Supplement Material), which shows a drastic

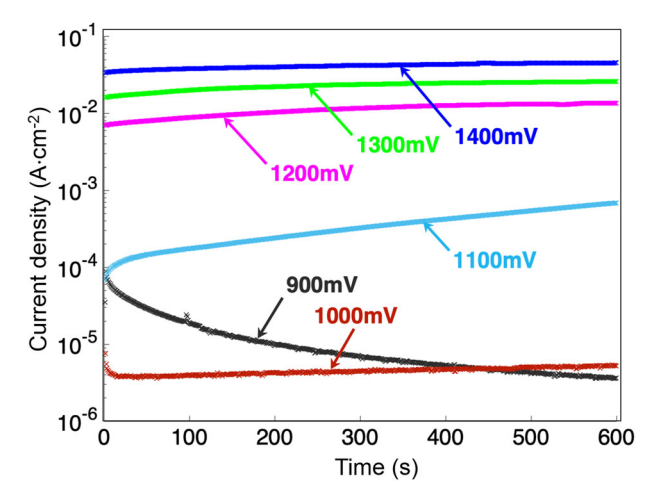


Fig. 1 Anodic current density vs. time recorded at each applied potential. Decreasing current density with time to a low level at 900 mV indicates a passive condition. Increasing current density with time at 1000 mV indicates the onset of transpassive breakdown. All potentials are given with respect to Ag/AgCl (sat.)

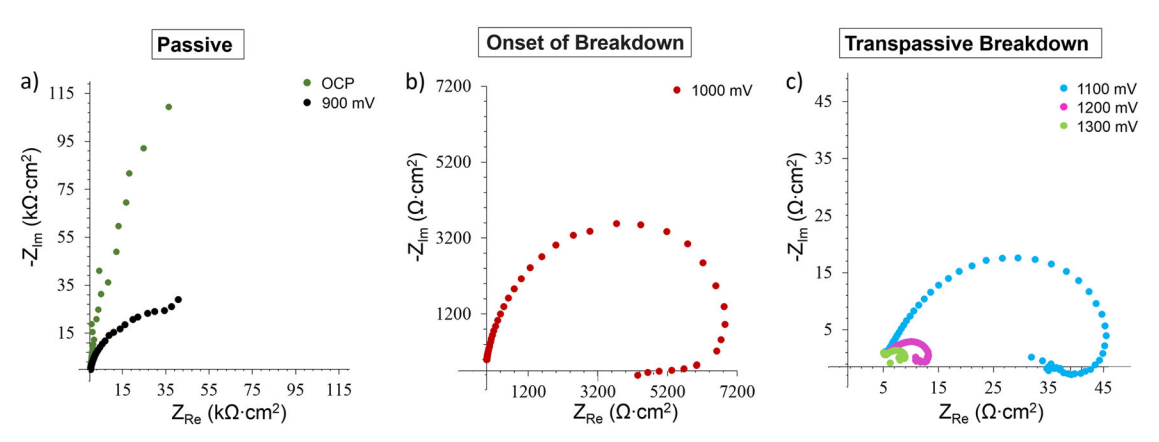


Fig. 2 Nyqvist plots of EIS spectra collected at OCP and step-wisely increased anodic potentials: **a** OCP and 900 mV; **b** 1000 mV; **c** 1100, 1200, and 1300 mV. All potentials are given with respect to Ag/AgCl (sat.). The spectra in the figures show **a** typical passive condition, **b** onset of breakdown, and **c** transpassive breakdown

decrease of the charge transfer resistance with increasing potential from 900 to 1300 mV/ $_{\rm Ag/AgCI}$ (Table S1), suggesting that the passive film became highly defective and eventually lost its protective ability.

In-situ and operando XRR analysis

Figure 3 shows the XRR data obtained at the OCP and increasing applied potentials. At potentials up to 1300 mV/_{Ag/AgCl}, the curves showed distinct and broad fringes (Fig. 3a-e), indicating the presence of two (or more) interfaces, with broader fringes implying thinner surface layers. At 1400 mV/_{Ag/AgCl}, no fringe was seen (Fig. 3f), suggesting that the surface became too rough for the reflectivity measurement. Analysis of the XRR data was performed by fitting the curves using a two-layer surface film model, consisting of a low-density outer layer (passive film) and an underlying high-density inner layer (alloy surface layer) on top of the bulk substrate, as illustrated in Fig. 3g. The two-layer model used for curve fitting assumes that the passive film and the alloy surface layer are uniform, neglecting possible differences in the passive film between the ferrite and austenite phases. The inner and outer part of the passive film, including hydroxides, is considered as one oxide layer. Satisfactory fitting is seen in Fig. 3 from the excellent matching between the measurement and the simulation using the fitting results. Table 1 summarizes the fitting results, i.e., the thickness, density and roughness of the two layers. The data obtained at 1400 mV/_{Aq/AqCI} did not show clear fringes so the fitting was not reliable.

At the OCP, the two layers had a similar thickness of ca. 2 nm, and the density of the passive film was 5.2 g/cm³, which is approximately the density of Fe and Cr oxides (5.22 g/cm³ for Cr₂O₃ and 5.24 g/cm³ for Fe₂O₃). The density of the alloy surface layer was 8.3 g/cm³, which is higher than that of the bulk material (7.8 g/cm³). With increasing applied potential, the thickness of both layers increased slightly, and the density of the passive film decreased whereas the density of the alloy surface layer increased (Table 1). The simultaneous increase in thickness and decrease in density of the passive film suggest an increased amount of vacancies in the oxide layer at higher potentials. Meanwhile, the increased density of the alloy surface layer implies an enrichment of heavier elements, in this case Ni (8.9 g/cm³) and Mo (10.2 g/ cm³). Apparently, the density became higher than that of pure Ni, suggesting that also Mo became enriched in the alloy surface layer at the high potentials. At 1300 mV/_{Aq/AqCI}, the density of the alloy surface layer decreased slightly, accompanied by a roughness increase.

In situ detection of dissolved metal elements by XRF

The XRF data are summarized in Fig. 4, showing signals from the K_{α} -absorption and K_{β} -absorption edges for Fe, Ni, Mo, and Cr, indicating metal dissolution. No signal of any dissolved element was detected during exposure at the OCP, and first signals (inset in Fig. 4a) were detected at $900\,\text{mV/}_{Ag/AgCl}$ showing little Fe dissolution. The signals were of the same intensity at $1000\,\text{mV/}_{Ag/A}$ further increase of the potential increased the signal intensity of Fe, but no other element was detected until $1200\,\text{mV/}_{Ag/AgCl}$, at which small signals of Ni and Mo were also detected (Fig. 4b, c). At $1300\,\text{mV/}_{Ag/AgCl}$, the signal intensity of Fe, Ni, and Mo increased significantly, and Cr was also detected (Fig. 4d), indicating rapid Cr dissolution. The signals of Fe, Cr, Ni, and Mo were greatly enhanced at $1400\,\text{mV/}_{Ag/AgCl}$, implying the active dissolution of the metal without a protective barrier.

For a visual representation of the amount of metal dissolution, the normalized data (total of dissolved elements = 100%) was plotted in Fig. 5a showing the percentage of the dissolved elements as a function of applied potential. Fe was the dominant dissolving element up to 1300 mV/_{Ag/AgCl}, whereas Cr dissolution increased and became similar to Fe at 1400 mV/Ag/AgCI. The dissolution of Ni was little and the dissolution of Mo was the lowest at all potentials. Figure 5b shows the data as relative increase (height ratio normalized to the peak of Fe at $1000\,\text{mV/}_{Ag/AgCl}$) of the cross-section corrected signal intensity for the dissolving metal elements. Clearly, Fe was the mostdissolving element ('dealloying') in the potential region from 1000 to 1200 mV/_{Ag/AgCl}. Calculation of absolute amounts of the dissolved elements was not attempted, because lack of detailed knowledge of the concentration gradients around the electrode and the complexity of computation of secondary fluorescence events in the electrolyte and the sample. It should be noted that the sensitivity for detection of Cr is low due to its low cross-section and emission energy, so minor Cr dissolution at potentials below 1300 mV/_{Ag/AgCI} cannot be ruled out. In contrast, the sensitivity to Mo is high due to its high cross-section, so the information about Mo has high confidence.

GIXRD of the outermost surface

The GIXRD results are summarized in Fig. 6. The full spectra of all indexed peaks and a short discussion were reported elsewhere. All peaks of the austenite and ferrite were seen to shift to lower Bragg angles (larger d-spacing), with the ferrite showing larger shifts. Moreover, the peaks became distorted and broadened after polarization to 1400 mV/_{Ag/AgCl}, more for the ferrite than the austenite. The largest shift occurred on (211)-oriented ferrite



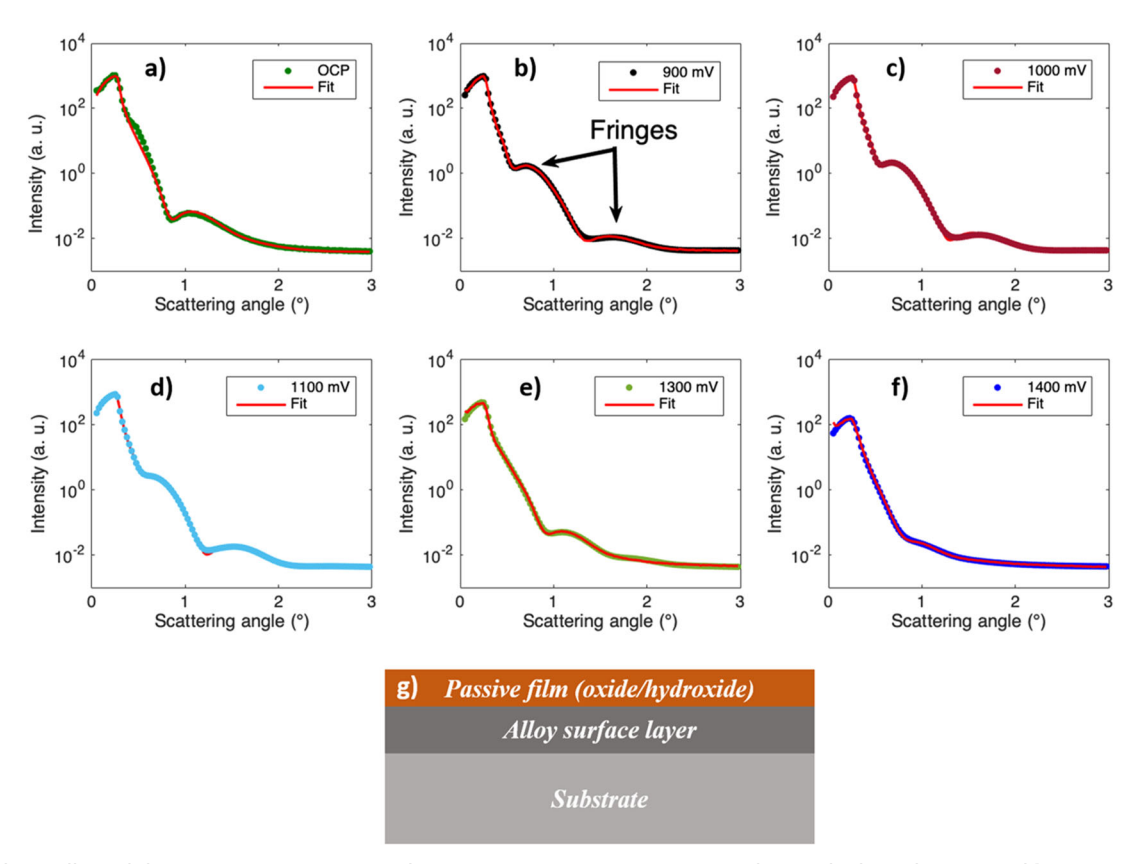


Fig. 3 XRR data collected during exposure in 1 M NaCl at room temperature: a at OCP, and at applied anodic potential b 900 mV, c 1000 mV, d 1100 mV, e 1300 mV, and f 1400 mV, respectively. All potentials are given with respect to Ag/AgCl (sat.). g The two-layer model used for curve fitting. The fringes of the XRR curves are originated from X-ray reflections at the surface and the interfaces of the oxide and the alloy surface layers, and the red lines show simulation using the fitting data

 Table 1.
 Fitting results of XRR data obtained during exposure to 1 M NaCl solution at room temperature, at each step-wisely increased anodic potential

Potential (mV _{Ag/AgCl})	Alloy surface laye	r		Passive film						
	Thickness (nm)	Density (g/cm³)	Roughness (nm)	Thickness (nm)	Density (g/cm³)	Roughness (nm)				
ОСР	2.5	8.3	0.5	2.1	5.2	0.7				
900	2.6	8.8	0.5	3.3	5.0	0.9				
1000	2.8	9.1	0.5	3.7	5.0	0.9				
1100	3.0	9.0	0.6	3.8	4.7	1.0				
1200	3.4	9.1	0.6	4.0	4.3	1.2				
1300	3.8	8.7	0.7	3.3	4.0	1.5				
1400	Fringes in the spectrum became unclear									

The systematic error of the measurement was 2–5%. Using Genx program, the error bar was estimated to be <0.1 nm for the thickness and \leq 0.01 g/cm³ for the density of the two surface layers, and \leq 0.02 nm for the roughness

grains and on (311)-oriented austenite grains (Fig. 6a). Numerous small peaks were detected which were indexed as Cr-oxides and Fe-oxides having varying compositions (a mix-compound consisting of Cr-oxide, Fe-oxide, Fe-Mo-oxide, Cr-Mo-oxide, and Fe-Mn-oxide species), with the peaks for Cr-oxides showing strongest signals (Fig. 6b). Some additional peaks other than those of indexed Cr-oxides and Fe-oxides were detected which, however, were not allocated to any compound (denoted as "new oxide" in Fig. 6b, d). The oxide peaks had a high peak-width-to-height ratio, indicating nanometer-sized grains. The peaks for all oxides became broader and distorted with increasing potential. The

peaks for Cr-oxides shifted to higher Bragg angles whereas no considerable peak shift occurred for Fe-oxides (Fig. 6c, d). All peak-signal intensities (bulk phases and oxides) decreased during polarization to $900\,\text{mV/}_{Ag/AgCl}$ and then increased after polarization to $1400\,\text{mV/}_{Ag/AgCl}$.

DISCUSSION

For low and medium-alloyed stainless steels, an abrupt increase of current density in the polarization curves occurs at low potentials indicating passivity breakdown, known as the breakdown/pitting

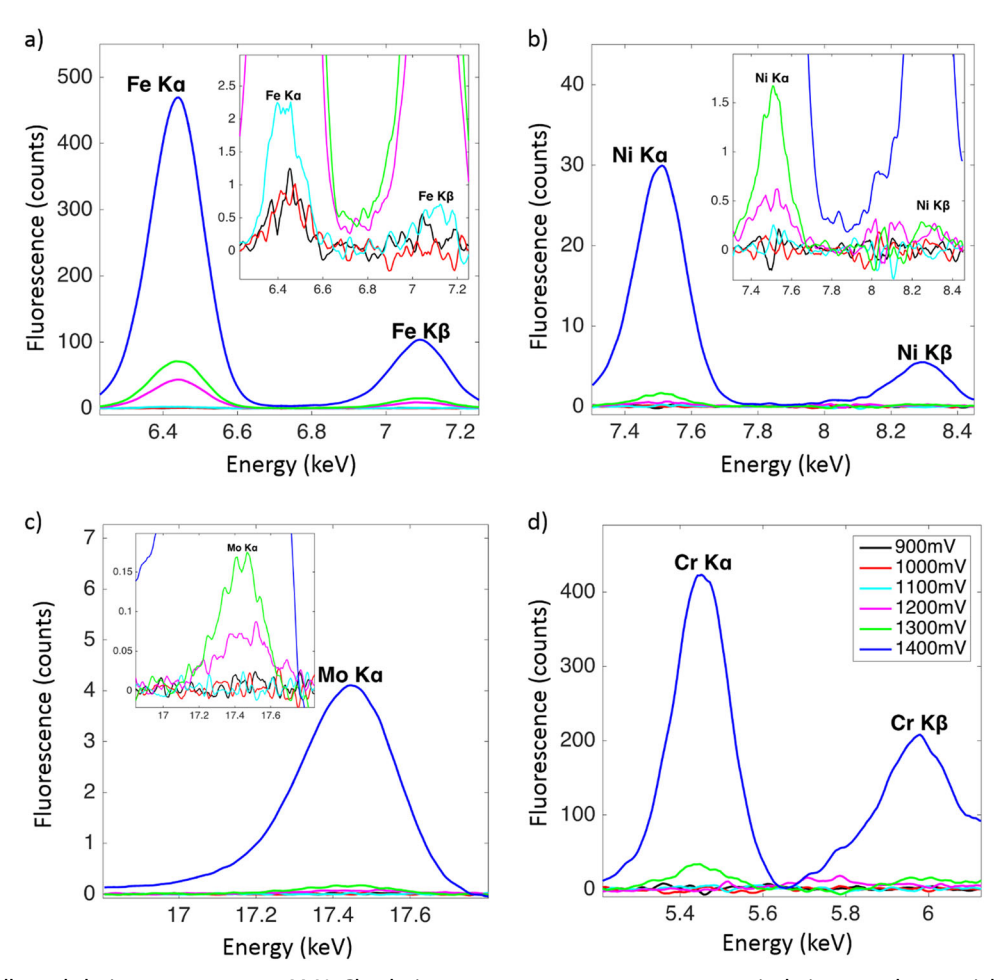


Fig. 4 XRF data collected during exposure to 1 M NaCl solution at room temperature at step-wisely increased potentials showing detected elements in the electrolyte: **a** Fe, **b** Ni, **c** Mo, and **d** Cr, respectively. All potentials are given with respect to Ag/AgCl (sat.). The signal peaks indicate enhanced dissolution of the elements (no peak was detected in the passive condition except a small one for Fe)

potential. Passivity breakdown of highly alloyed stainless steels, in contrast, is usually due to transpassive dissolution at higher potentials. The transpassive state is characterized by rapid dissolution of metal elements, which is commonly believed to be due to the transition of stable $\text{Cr}^{3+}\text{-}\text{oxide}$ to soluble $\text{Cr}^{6+}\text{-}\text{species.}^{1-3,9-11,14,34-37}$ In the PDM, the prediction of transpassive breakdown potential is based on the $\text{Cr}^{3+} \to \text{Cr}^{6+}$ reaction. 8,81,82 However, the electrochemical behavior of Crcontaining multi-element alloys differs largely from that of pure Cr, and there are large variations in the transpassive breakdown potential of different kinds of stainless steels. Environmental conditions, such as pH, temperature and chloride concentration, all have an influence on the breakdown process. It is well known that chloride ions in the solution attack the passive film in different ways, 9,37,38 and therefore lower the passivity breakdown potential.

The combined electrochemical measurements and operando synchrotron X-ray analyses presented provide comprehensive information about the transpassive breakdown of the super duplex stainless steel in 1 M NaCl solution. The current transients and ElS measurements showed the onset of the transpassive breakdown at 1000 mV/Ag/AgCl; however, Fe was the dominant dissolving element, and the passive film became thicker up to 1200 mV/Ag/AgCl. Moreover, oxygen evolution reaction may have contributed to the increased current whose kinetics increase rapidly with increasing potential. So, it is questionable to define the transpassive breakdown potential only based on the increased anodic current. At 1200 mV/Ag/AgCl, dissolution of Ni and Mo was detected, and minor Cr dissolution might also be possible, but the

passive film was still present on the surface. Rapid Cr dissolution was only detected at potentials ≥1300 mV/_{Ag/AgCI} together with rapid Fe dissolution. Under this condition, the passive film became thinner and the density became lower, indicating true passive film breakdown. Therefore, aside from electrochemical evidence, structural and/or chemical evidences are also required for a more accurate delineation of the passivity breakdown. In fact, the passivity breakdown is a transition from passive to transpassive state, which involves electrochemical processes, starting at lower potentials, and structural and compositional changes of the passive film, occurring at higher potentials, spanning over a range more than 200 mV. Hence, the transpassive breakdown occurs rather over a potential range than at a fixed potential.

The fact that true passive film breakdown of the super duplex stainless steel occurred at such high polarization potentials implies high stability of the passive film in the chloride solution. Existing models assuming that pure Cr₂O₃ is formed on stainless steel are not sufficient to describe the observations.⁸³ Synergistic effects between Cr, Ni, Mo, and N on the passivity need to be considered to explain the superior corrosion resistance of such alloys.^{3,41} In practice, the likelihood that the cathodic reaction in natural environments can lift the corrosion potential to the transpassive breakdown potential range is little, and therefore the transpassive breakdown is not likely to occur on the super duplex stainless steel under normal exposure conditions. However, the transpassive breakdown is a concern under extreme conditions, such as evaluated temperature, atmospheric corrosion exposures, and aggressive solutions inside crevices.⁸⁵ Here, the transpassive



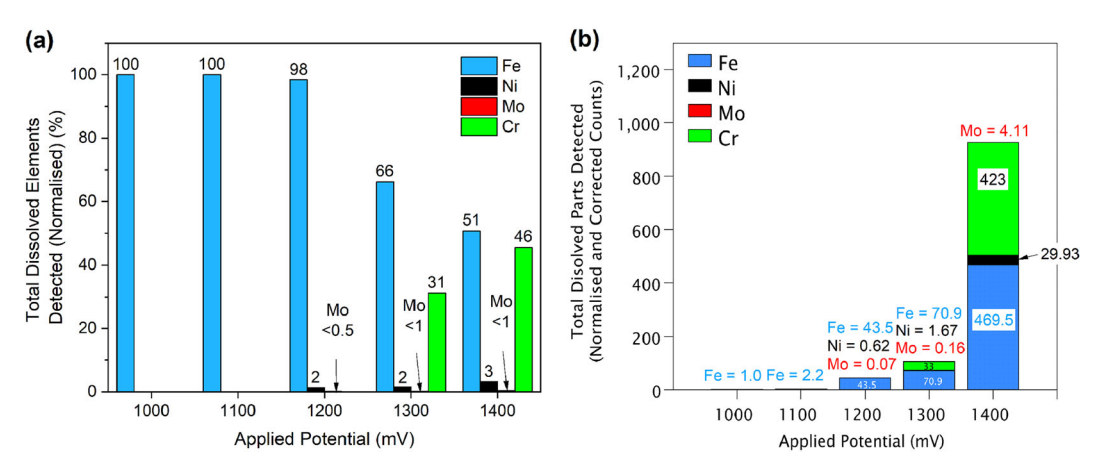


Fig. 5 XRF data of detection of dissolved Fe, Cr, Ni, and Mo in 1 M NaCl at room temperature during anodic polarization at applied potentials. The bar chart at the right shows proportions of dissolved elements after correction of the cross-sections and normalization to the signal of Fe at 1000 mV (Fe = 1). The bar chart at the left shows the data normalized to 100% at each potential. All potentials are given with respect to Ag/AgCl (sat.)

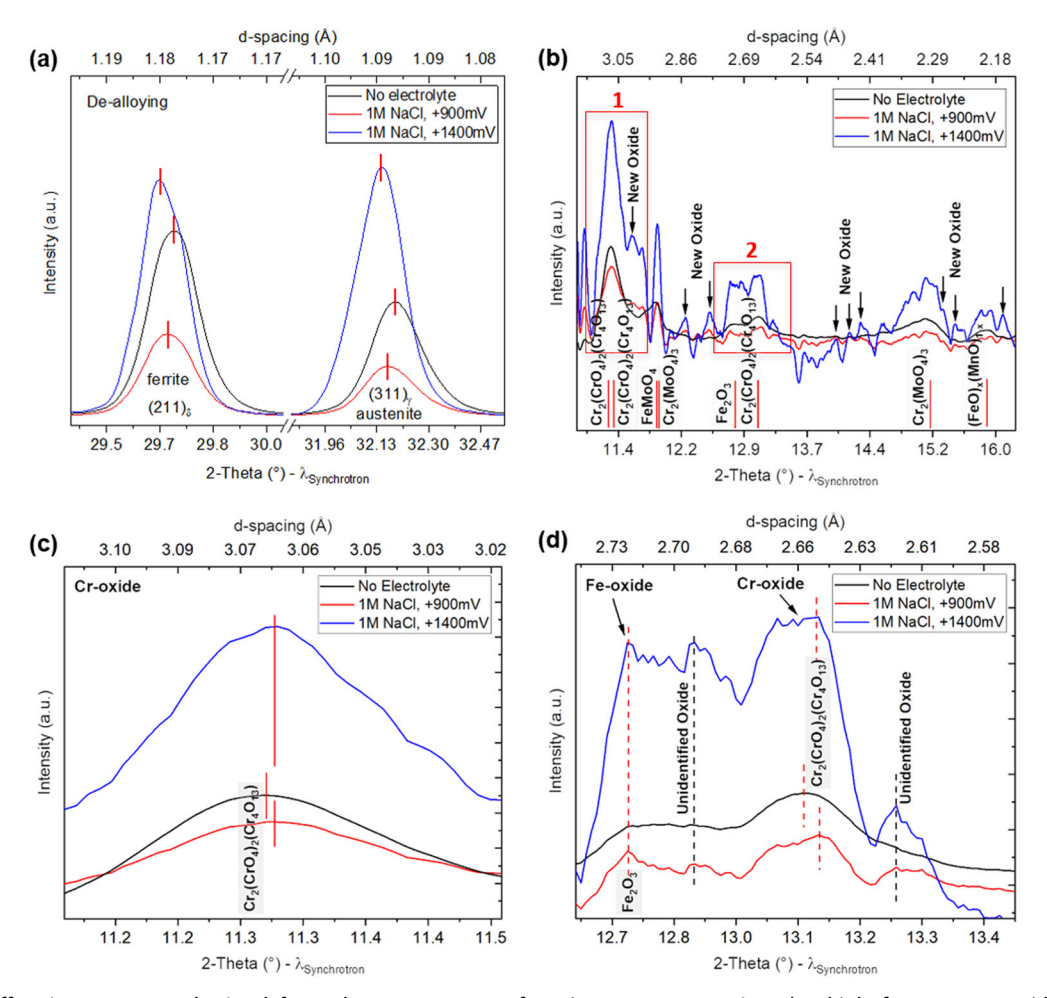


Fig. 6 GIXRD diffraction patterns obtained from the outermost surface (~50 nm penetration depth) before exposure (dark line), during exposure to the electrolyte after polarization (but still applied) to 900 mV/_{Ag/AgCI} (red line), and after termination of the polarization to 1400 mV/_{Ag/AgCI} (blue line): **a** showing peak shifts of ferrite and austenite phases indicating preferential dissolution of Fe, **b** showing peak-signal intensity increase of the passive film and the formation of new peaks, **c** magnified view of the highlighted region denoted as no. 1 in **b** showing peak shift for Cr-oxide indicating lattice expansion, and **d** magnified view of the highlighted region no. 2 in **b** showing no change of the peak positions for Fe-oxide but for Cr-oxide, and also the formation of new peaks indicating new oxide/hydroxide constituent(s)

breakdown potential range can be regarded as the ultimate limit for the passive condition.

The passive films formed on stainless steels are usually a few nanometers thick, ¹⁴ and the film thickness increases slightly with increasing potential in the passive regime. Ni enrichment in the alloy surface layer beneath the passive film was observed to be in a narrow range (a few nm in depth).^{86–88} The operando synchrotron XRR analysis provided information about the thickness and density of the passive film and the alloy surface layer (with high accuracy), as well as their changes during the transition from passive to transpassive state. The thickness of the passive film increased in the passive region. During the transition from passive to transpassive state occurring in the potential range of 1000–1200 mV/_{Ag/AgCl}, the thickness further increased whereas the density decreased with increasing potential, which was due to enhanced anodic dissolution of mainly Fe. The dissolution process was associated with defect formation in the oxide whereby the density became lower. Hence, the increased anodic dissolution was most likely caused by the increased number of vacancies in the oxide that facilitated ionic transport across the oxide layer. At potentials ≥1300 mV/_{Ag/AgCl}, the oxide dissolution rate exceeded its formation rate leading to the thinning of the passive film as evidenced by the enhanced anodic dissolution of the metal elements (XRF data) and the eventual removal of the passive film (XRR data).

Another key observation is that the anodic polarization is accompanied by compositional and structural variations of the alloy surface layer beneath the passive film. The XRR results showed that the density of the alloy surface layer was already higher than that of the bulk material at the OCP, and it increased significantly with increasing potential up to 1000 mV/_{Aq/AqCl}. This means that an enrichment of the heavier elements (Ni and Mo) must have occurred, due to the preferential Fe dissolution. During the transition from passive to transpassive state in the higher potential range (1000-1200 mV/Ag/AgCI), the density reached to 9.1 g/cm³, which suggests that not only Ni but also Mo (heavier than Ni) was enriched in the alloy surface layer. This is also supported by the XRF results showing little dissolution of Mo, which was much lower than its proportion in the alloy. Enrichment of Ni beneath the passive film was observed on 304 L and 316 L stainless steels and ascribed to preferential oxidation of Fe and Cr at the oxide/metal interface. 86,87 It is well known that the addition of Mo into stainless steel enhances the resistance to localized corrosion, in particular, the repassivation ability.³ However, because of the difficulty in the surface analysis, only a few literature reports could show the presence of Mo in the surface, mostly as high valence (Mo⁴⁺ and Mo⁶⁺) species in the passive film and also as metallic Mo beneath the passive film of stainless steels. 14,41,42 There are hypotheses, e.g., mixed nitride theory, about the synergistic effects between Mo, Cr, Ni, and N to the passivity in order to explain the high corrosion resistance of the alloys containing these elements.^{3,41} Our results suggest that there is an enrichment of metallic Ni and Mo in the alloy surface layer underneath the passive film, and they may, together with Cr and N, indeed form mixed nitrides that are stable and retard the metal dissolution, contributing to the high corrosion resistance of the super duplex stainless steel. These observations support the synergism of the alloying elements believed to reduce the dissolution propensity. In a nutshell, not only the passive film but also the underlying alloy surface layer plays an important role in the high corrosion resistance of stainless steels.

The passive condition of a passivating metal is maintained when the competing oxide formation and dissolution processes are in equilibrium, and transpassive breakdown occurs when the oxide dissolution is faster than its formation. For multi-element alloys, the dissolution of the passive film is a complicated process because the dissolution propensity is different for each alloying element and for their oxides/hydroxides, and the composition of

the passive film changes with applied potential. 1-3,8-11 For the super duplex stainless steel, preferential Fe dissolution is accompanied by Cr enrichment in the passive film, which explains its resistance against rapid metal dissolution up to the potential for film breakdown despite the onset of transpassive breakdown at 1000 mV/_{Ag/AgCI}. The passive film remained on the surface but became more defective, which facilitates ionic transport due to an increased vacancy density. Only when the potential was at \geq 1300 mV/ $_{Ag/AgCl}$, the passive film dissolved rapidly, most probably due to the oxidation of stable Cr3+-compounds to soluble Cr⁶⁺-species, allowing active dissolution of the metal. GIXRD showed that there is a shift of Cr-oxide peaks which indicates the change of the lattice size of the oxide crystals. The broadening and distortion of all the oxide peaks were associated with the compositional changes due to preferential dissolution of Fe-oxides and enrichment of Cr-oxides, and/or formation of new oxides during and after the anodic polarization. It is not surprising that new oxide/hydroxide compounds were formed as the surface was chemically altered by anodic polarization to the transpassive domain.

The shift of ferrite and austenite peaks to lower Bragg angles is a clear sign for lattice expansion due to the preferential dissolution of Fe as confirmed by the XRF analysis. The dissolution of Fe led to lattice expansion of the grains in the surface layer. The observed asymmetric shapes of the ferrite peaks indicate more Fedissolution from the ferrite than the austenite, implying selective attack occurred on the ferrite, which was confirmed by postpolarization analysis of the surface using SEM and electron backscatter diffraction (EBSD).⁸⁴ It seems that the enhanced Fe dissolution was the first step in the corrosion initiation, and transpassive breakdown initiated first on ferritic grains and then spread over austenitic grains.⁸⁴ The propensity to Fe dissolution increased with increasing potential leading to the development of more lattice strains. The strain, however, may have also been introduced by the different strain/stress evolution in both phases. which could have altered the residual stress state of the outermost surface and thus the selective dissolution of ferrite.

There are controversies in the literature regarding the structure (amorphous vs. crystalline) of the passive films on stainless steels due to different surface conditions and the use of different analytical techniques. ^{13,14,24–30} The GIXRD results in this study clearly showed that the air-formed, native oxide film on the super duplex stainless steel was crystalline with some amorphous fractions, and the oxide remained during the anodic polarization before removal.⁸⁴ The passive film was composed of mainly Croxides and Fe-oxides with some substitutes of Mo and Mn, having nanometer-sized grains. The anodic polarization led to the loss of crystallinity, possibly due to increased vacancies, compositional changes due to selective dissolution, and/or formation of new oxides/hydroxides having an amorphous structure. Upon termination of the electrochemical polarization at 1400 mV/_{Aq/AqCl}, at which passive film dissolution occurred, similar Cr-oxides and Feoxides were detected on the sample surface. The increased diffraction signals of the crystalline oxide peaks as well as the background indicate an increased amount of oxides. It is possible that the re-formed surface film contained some deposited Cr- and Fe-containing compounds since the rapid dissolution generated a high concentration of Fe and Cr in the vicinity of the surface. The results indicate a strong tendency of the super duplex stainless steel to re-passivate after breakdown in 1 M NaCl solution at room temperature.

In summary, the combined electrochemical measurements and operando synchrotron X-ray analyses have shown that the passivity breakdown of the 25Cr–7Ni super duplex stainless steel in 1 M NaCl solution is a transition from passive to transpassive state, spanning over a potential range more than 200 mV. The breakdown involves chemical/electrochemical reactions as well as compositional and structural changes of the passive film and the



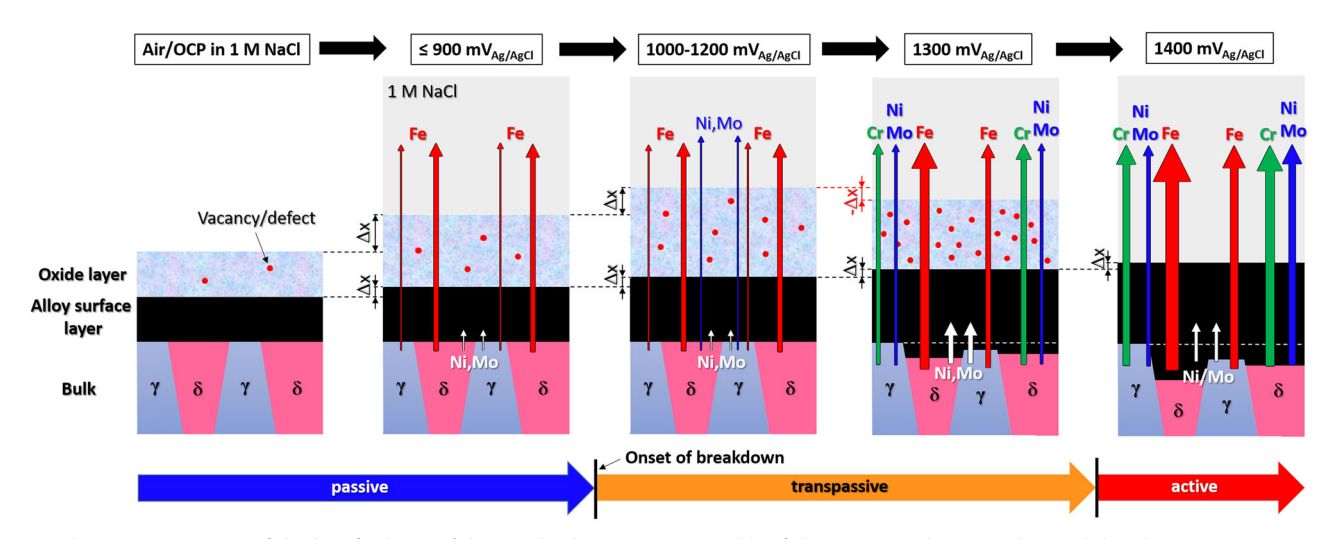


Fig. 7 Schematic summary of the key findings of this work. The increasing width of the arrows indicates enhanced dissolution associated with increasing potential. Selective dissolution of ferrite is illustrated as a recession in vertical direction of the ferrite phase (δ) in comparison with the austenite phase (γ) being less dissolved. The thickness of the arrows indicates the flux/extent of dissolution

underlying alloy surface layer. The core findings are summarized schematically in Fig. 7. The anodic polarization to high potential in the range of $1000-1200\,\text{mV/}_{Ag/AgCl}$ leads to preferential Fe dissolution, occurring more on the ferrite than on the austenite phase. Meanwhile, the passive film becomes thicker, from ca. 2 nm to ca. 4 nm, but less dense due to anodic Fe dissolution. The alloy surface layer beneath the passive film has a thickness of a few nanometers, which increases slightly upon anodic polarization, and its density increases due to anodic enrichment of Ni and Mo. The true passive film breakdown associated with rapid Cr dissolution takes place at $\geq 1300\,\text{mV/}_{Ag/AgCl}$. The passivity of the super duplex stainless steel is the ability to sustain the structural integrity of the surface oxide and the underlying alloy surface layer.

METHODS

Material used and experimental setup

The material used was a solution-annealed 25Cr-7Ni (UNS S32750) grade super duplex stainless steel with the chemical composition given in Table 2, provided by AB Sandvik Materials Technology, as a 10 mm thick plate. The microstructure consisted of ferrite and austenite phases in similar fractions. Electrochemical (current transients and EIS), in situ and operando synchrotron X-ray measurements were performed at the beamline ID03 at the European Synchrotron Radiation Facility (ESRF). Hat-shaped samples, as specified in Fig. 8a, were manufactured from the plate material so that the surface was parallel to the normal plane of the plate. The samples were ground with SiC paper successively down to 4000-grit size, followed by mechanical polishing down to ¼ µm diamond paste in an apparatus to avoid sample edging. The samples were further fine-polished using OPS oxide-active polishing suspension (Struers, Denmark) to reduce the surface roughness. Then the surface was re-polished using $\frac{1}{4}$ μm to remove the chemically altered surface due to the OPS polishing. The samples were cleaned and dried and then stored in dry ambient air prior to the experiment. The total time elapsed from storage to measurement time was one week. The sample was mounted in an electrochemical cell made of polyether ether ketone (PEEK), schematically shown in Fig. 8a. The cell was translucent to the X-ray beam allowing electrochemical and X-ray measurements on the metal surface, as schematically illustrated in Fig. 8b-d. The cell consisted of the sample as the working electrode, a glassy carbon counter electrode, a saturated Ag/AgCl reference electrode, and two polytetrafluoroethylene (PTFE) tubes for electrolyte supply and drainage. The electrolyte was 1 M NaCl solution prepared from analytical grade chemical using ultra-pure water (Milli-Q), and its pH was ~5.5. All electrodes were connected to a Metrohm Autolab potentiostat.

Table 2. Chemical composition (wt%) of 25Cr–7Ni (UNS S32750) super duplex stainless steel												
С	N	Р	S	Si	Mn	Ni	Cr	Мо	Cu	Fe		
0.017	0.27	0.022	0.001	0.6	0.77	6.9	24.9	3.87	0.26	Bal.		

Measurement procedures

The X-ray measurements consisted of XRR, XRF, and GIXRD using a photon energy of 20.5 keV and a beam size of 90 μm × 35 μm. These measurements were carried out to measure compositional and structural changes occurring on the passive film and the underlying alloy surface layer during exposure to the electrolyte without and with anodic polarization. An overview of all experiments performed is summarized in Fig. 9. During the measurement, the sample was rotated with a step size of 0.01° (0.0018 Å^{-1}) with respect to the beam. GIXRD was used to obtain near-surface structural information. The X-ray beam was impinged on the sample surface with an incident angle of 1°, producing signals emanating from ca. 20-50 nm below the surface. First, GIXRD was measured in ambient air (no electrolyte) to characterize the air-formed surface oxide film and aspolished microstructure of the material, with a momentum transfer (q-space) range of 1.97–6.75 ${\mathring{A}}^{-1}$ corresponding to the 2-Theta range of 10.9-37.92°. Then, the electrolyte was filled into the electrochemical cell having a reservoir volume of ca. 3 mL, and metallic elements in the electrolyte were measured using XRF for background subtraction. The open-circuit potential (OCP) was monitored for 10 min to reach a nearsteady-state condition. XRR, EIS, XRF, and XRD measurements were done in sequence, first without and then with applied potential, as shown in Fig. 9. At each polarization step (600, 900, 1000, 1100, 1200, 1300, 1400 mV/ mV/_{Ag/AgCl}), the current was recorded for 10 min to get the current transients and also to reach a near-steady state condition. EIS measurements were performed in the frequency range of 10^4 – 10^{-2} Hz with a perturbation amplitude of 10 mV, using the Autolab potentiostat (Metrohm). The data were processed using NOVA software.

The completion time for each measurement sequence was ca. 60 min without XRD and 75 min with an XRD measurement. The measurement time of a single XRR scan was 5–10 min, capturing signals at incidence angles between 0 and 3°. The XRR curves were analyzed to obtain thickness and density of the surface layers, using the two-layer model (see Fig. 3g) for the curve fitting done in the same way as described previously. ^{78–80} The synchrotron-based XRR is a very sensitive technique for measurement of the thickness and density of thin surface films. For a thin film on a flat substrate, the period of the fringes depends on the thickness of the film, the amplitude of the fringes depends on the electron density difference between the film and the substrate, while the general decay of the reflectivity curve, and the dumping of the oscillation depend

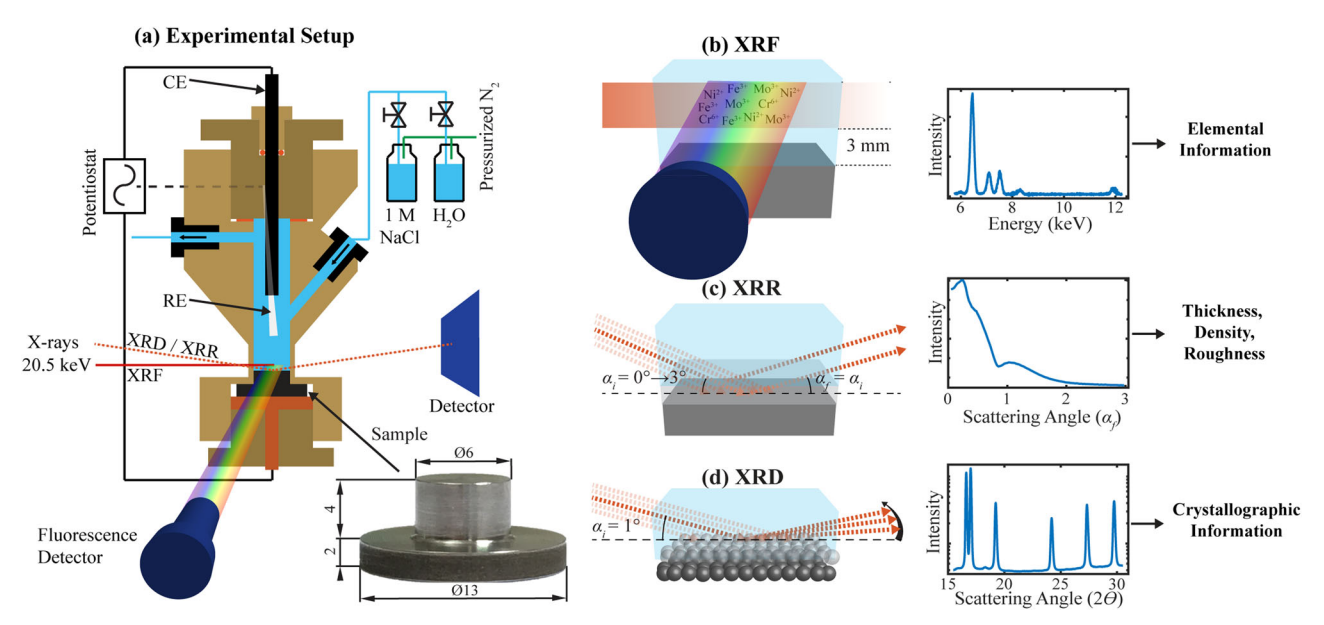


Fig. 8 Schematic illustration of the experimental setup, **a** showing the three-electrode electrochemical cell, the sample dimensions (in mm) and the tubes for the inlet and outlet of gas or liquid, **b** depicting the XRF, **c** XRR, and **d** GIXRD measurements. The cell consists of a saturated Ag/AgCI reference electrode (RE), a glassy carbon counter electrode (CE), and the sample as the working electrode (WE), all connected to a potentiostat

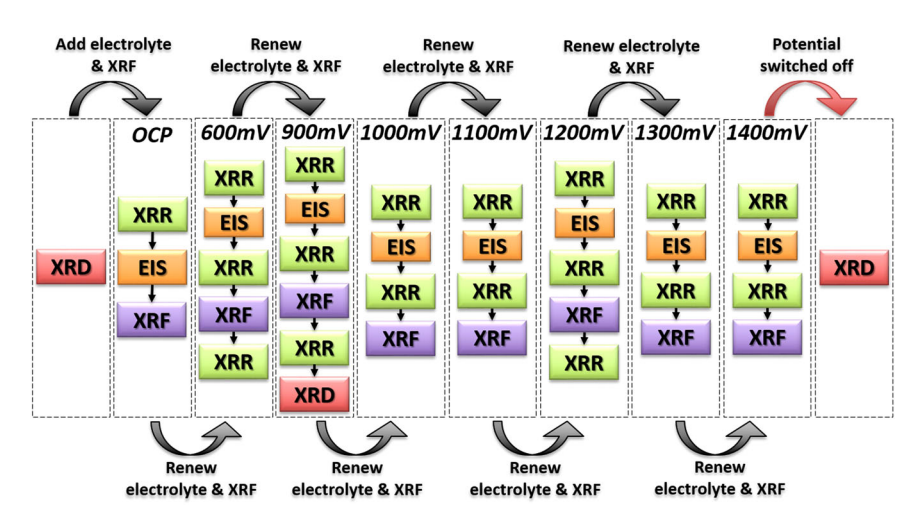


Fig. 9 Overview of the measurements carried out in the consecutive order

on the roughness of the surface or interface. The XRR method gives a good estimate for the thickness, density, and roughness of a surface layer since these parameters have a strong influence on the reflectivity. The XRR is mainly sensitive to the derivative of the material refractive index, which depends in first approximation on the electron density of the materials. This leads to an extremely high absolute accuracy for the thickness down to Å, as often reported in the literature, and also a high accuracy of the change in the density of the thin layer on the surface. XRF measurements were carried out to detect signals from Fe, Ni, Mo, and Cr in the electrolyte. The incident X-ray beam was oriented parallel to and centered 3 mm above the sample surface, and the dissolved elements in the electrolyte were detected within an ellipsoidal volume of 90 µm in length and 35 µm in height. Collection of the XRF spectra took ca. one minute. Characteristic emission peaks for Fe, Ni, Cr, and Mo were assigned by calibrating the detector channels using a number of reference electrolyte samples and then identifying the measured peaks according to accepted values.⁸⁸ The XRF spectra obtained at each polarization step were compared after background subtraction to demonstrate the increasing anodic dissolution of each of these elements upon increased polarization potential. GIXRD

was done to obtain surface-sensitive structural information for the following sample conditions: (i) in air, (ii) during polarization at 900 mV in the electrolyte, and (iii) after termination of polarization at 1400 mV in the electrolyte. Phase identification from the XRD data was carried out using DIFFRAC.EVA analysis software (Bruker) with the aid of the ICDD reference database. Following PDF card numbers were found as the phases showing the best match: 01-080-2473 (Cr-oxide), 00-022-0629 (FeMoO₄), 01-088-2359 (Fe₂O₃), 01-078-1654 (Cr₂(MoO₄)₃), 04-016-6641 (austenite) and 00-006-0696 (ferrite).

DATA AVAILABILITY

The data that support the findings of this study are available from the corresponding author upon reasonable request.

ACKNOWLEDGEMENTS

The authors are grateful for the financial support by the Swedish Research Council (Vetenskapsrådet) through the project grant no. 2015-04490 and 2015-06092. ESRF,



Grenoble, France, is greatly acknowledged for the access to the beam time at ID03 beam line and support for the synchrotron experiment.

AUTHOR CONTRIBUTIONS

M.L. and C.Ö. conducted the experiments, analyzed the data, and wrote the manuscript. J.E. and G.H. conducted the experiments, analyzed the data, and contributed to the preparation of the manuscript. W.L. and L.R. conducted the experiments. F.C. and R.F. prepared the synchrotron experimental setup and contributed to the preparation of the manuscript. E.B. and U.K. provided the duplex stainless steel and contributed to the discussion of the data. E.L. supported the preparation for the experiments and contributed to the preparation of the manuscript. J.P. designed and planned, conducted, and analyzed the experiments and wrote the manuscript.

ADDITIONAL INFORMATION

Supplementary information accompanies the paper on the *npj Materials Degradation* website (https://doi.org/10.1038/s41529-019-0084-3).

Competing interests: The authors declare no competing interests.

Publisher's note: Springer Nature remains neutral with regard to jurisdictional claims in published maps and institutional affiliations.

REFERENCES

- Macdonald, D. D. The point defect model for the passive state. J. Electrochem. Soc. 139, 3434–3449 (1992).
- Macdonald, D. D. Passivity—the key to our metals-based civilization. Pure Appl. Chem. 71, 951–978 (1999).
- 3. Marcus, P. (ed.) Corrosion Mechanisms in Theory and Practice. Chap. 3–5, (CRC Press, Taylor and Francis, Boca Raton, 2011).
- 4. Cahn, R. W., Haasen, P., & Kramer, E. J. (eds). *Materials Science and Technology*. (Wiley. Hoboken. 2000).
- Schmuki, P. From bacon to barriers: a review on the passivity of metals and alloys. J. Solid State Electrochem. 6, 145–164 (2002).
- Stratmann, M. & Frankel, G. S., in Encyclopedia of Electrochemistry. (eds Bard, A. J. & Stratmann, M.) (Wiley, Hoboken, 2003).
- Marcus, P. & Maurice V. in Materials Science and Technology. (ed. Marcus, P.) (Wiley, Hoboken, 2006).
- Macdonald, D. D. On the existence of our metals-based civilization. I. phase space analysis. J. Electrochem. Soc. 153, B213–B224 (2006).
- Marcus, P., Maurice, V. & Strehblow, H.-H. Localized corrosion (pitting): a model of passivity breakdown including the role of the oxide layer nanostructure. *Corros.* Sci. 50, 2698–2704 (2008).
- Macdonald, D. D. Passivity: enabler of our metals based civilisation. Corros. Eng. Sci. Technol. 49, 143–155 (2014).
- Soltis, J. Passivity breakdown, pit initiation and propagation of pits in metallic materials—review. Corros. Sci. 90, 5–22 (2015).
- Benoit, M. et al. Comparison of different methods for measuring the passive film thickness on metals. Electrochim. Acta 201, 340–347 (2016).
- Strehblow, H.-H., Maurice, V. & Marcus, P., in Corrosion Mechanisms in Theory and Practice. (ed. Marcus, P.) 235–326 (CRC Press Taylor & Francis Group, Boca Raton, 2011).
- Maurice, V. & Marcus, P. Progress in corrosion science at atomic and nanometric scales. Prog. Mater. Sci. 95, 132–171 (2018).
- Frankel, G. S. Pitting corrosion of metals—a review of the critical factors. J. Electrochem. Soc. 145, 2186–2198 (1998).
- Davoodi, A. et al. Integrated AFM and SECM for in situ studies of localized corrosion of Al alloys. Electrochim. Acta 52, 7697–7705 (2007).
- Davoodi, A. et al. Multianalytical and in situ studies of localized corrosion of en aw 3003 alloy influence of intermetallic particles. J. Electrochem. Soc. 155, C138–C146 (2008).
- Davoodi, A. et al. The role of intermetallic particles in localized corrosion of an aluminum alloy studied by an SKPFM and integrated AFM-SECM. J. Electrochem. Soc. 155, C211–C218 (2008).
- Bettini, E. et al. Influence of metal carbides on dissolution behavior of biomedical CoCrMo alloy: SEM, TEM and AFM studies. *Electrochim. Acta* 56, 9413–9419 (2011)
- Bettini, E. et al. Influence of grain boundaries on dissolution behavior of a biomedical CoCrMo alloy: in-situ electrochemical-optical, AFM and SEM/TEM studies. J. Electrochem. Soc. 159. C422–C427 (2012).

- Bettini, E. et al. Study of corrosion behavior of a 22% Cr duplex stainless steel: influence of nano-sized chromium nitrides and exposure temperature. *Electro-chim. Acta* 113, 280–289 (2013).
- Anantha, K. H. et al. Correlative microstructure analysis and in situ corrosion study of AlSI 420 martensitic stainless steel for plastic molding applications. J. Electrochem. Soc. 164. C85–C93 (2017).
- Anantha, K. H. et al. In situ AFM study of localized corrosion processes of tempered AISI 420 martensitic stainless steel: effect of secondary hardening. J. Electrochem. Soc. 164, C810–C818 (2017).
- McBee, C. L. & Kruger, J. Nature of passive films on iron-chromium alloys. Electrochim. Acta 17. 1337–1341 (1972).
- Tjong, S. C. TEM study of the passive film on iron-chromium alloys. J. Mater. Sci. Lett. 4, 6–8 (1985).
- Toney, M. F. et al. Atomic structure of the passive oxide film formed on iron. Phys. Rev. Lett. 79, 4282–4285 (1997).
- Maurice, V., Yang, W. P. & Marcus, P. XPS and STM study of passive film formed on Fe-22Cr (110) single-crystal surfaces. J. Electrochem. Soc. 143, 1182–1200 (1996)
- Maurice, V., Yang, W. P. & Marcus, P. X-ray photoelectron spectroscopy and scanning tunneling microscopy study of passive films formed on (100) Fe-18Cr-13Ni single crystal surfaces. J. Electrochem. Soc. 145, 909–920 (1998).
- Maurice, V. & Marcus, P. Passive films at the nanoscale. Electrochim. Acta 84, 129–138 (2012).
- Massoud, T. et al. Nanoscale morphology and atomic structure of passive films on stainless steel. J. Electrochem. Soc. 160, C232–C238 (2013).
- 31. Jiang, R. et al. Effect of time on the characteristics of passive film formed on stainless steel. *Appl. Surf. Sci.* **412**, 214–222 (2017).
- Zhang, X. & Shoesmith, D. W. Influence of temperature on passive film properties on Ni-Cr-Mo Alloy C-2000. Corros. Sci. 76, 424–431 (2013).
- Santamaria, M. et al. Photoelectrochemical and XPS characterisation of oxide layers on 316L stainless steel grown in high-temperature water. J. Solid State Electrochem. 19, 3511–3519 (2015).
- Song, G. Transpassivation of Fe–Cr–Ni stainless steels. Corros. Sci. 47, 1953–1987 (2005).
- Fattah-alhosseini, A. et al. The transpassive dissolution mechanism of 316L stainless steel. *Electrochim. Acta* 54, 3645–3650 (2009).
- Mishra, A. K. & Shoesmith, D. W. The activation/depassivation of nickel-chromium-molybdenum alloys: an oxyanion or a pH effect—Part II. Electrochim. Acta 102, 328–335 (2013).
- Tcharkhtchi-Gillard, E. et al. Kinetics of the oxidation of stainless steel in hot and concentrated nitric acid in the passive and transpassive domains. Corros. Sci. 107, 182–192 (2016).
- Al Saadi, S. et al. Passivity breakdown of 316L stainless steel during potentiodynamic polarization in NaCl solution. Corros. Sci. 111, 720–727 (2016).
- Diéz-Pérez, I., Sanz, F. & Gorostiza, P. In situ studies of metal passive films. Curr. Opin. Solid State Mater. Sci. 10, 144–152 (2006).
- Lutton, K. et al. Understanding multi-element alloy passivation in acidic solutions using operando methods. Electrochem. Commun. 80, 44–47 (2017).
- Olsson, C. O. A. The influence of nitrogen and molybdenum on passive films formed on the austeno-ferritic stainless steel 2205 studied by AES and XPS. Corros. Sci. 37, 467–479 (1995).
- 42. Olsson, C. O. A. & Landolt, D. Passive films on stainless steels—chemistry, structure and growth. *Electrochim. Acta* **48**, 1093–1104 (2003).
- Abreu, C. M. et al. Comparative study of passive films of different stainless steels developed on alkaline medium. *Electrochim. Acta* 49, 3049–3056 (2004).
- Femenia, M., Pan, J. & Leygraf, C. Characterization of ferrite austenite boundary region of duplex stainless steels by SAES. J. Electrochem. Soc. 151, B581–B585 (2004).
- Wang, H., Teeter, G. & Turner, J. Investigation of a duplex stainless steel as polymer electrolyte membrane fuel cell bipolar plate material. *J. Electrochem. Soc.* 152. B99–B104 (2005).
- Donik, Č. et al. XPS study of duplex stainless steel oxidized by oxygen atoms. Corros. Sci. 51, 827–832 (2009).
- Vignal, V. et al. Influence of the passive film properties and residual stresses on the micro-electrochemical behavior of duplex stainless steels. *Electrochim. Acta* 55, 7118–7125 (2010).
- 48. Luo, H. et al. Characterization of passive film on 2205 duplex stainless steel in sodium thiosulphate solution. *Appl. Surf. Sci.* **258**, 631–639 (2011).
- Luo, H. et al. The electrochemical behaviour of 2205 duplex stainless steel in alkaline solutions with different pH in the presence of chloride. *Electrochim. Acta* 64, 211–220 (2012).
- Vignal, V. et al. Passive properties of lean duplex stainless steels after long-term ageing in air studied using EBSD, AES, XPS and local electrochemical impedance spectroscopy. Corros. Sci. 67, 109–117 (2013).



- Wang, Y., Cheng, X. & Li, X. Electrochemical behavior and compositions of passive films formed on the constituent phases of duplex stainless steel without coupling. *Electrochem. Commun.* 57, 56–60 (2015).
- 52. Cui, Z. et al. Influence of temperature on the electrochemical and passivation behavior of 2507 super duplex stainless steel in simulated desulfurized flue gas condensates. *Corros. Sci.* **118**, 31–48 (2017).
- De Marco, R. & Veder, J.-P. In situ structural characterization of electrochemical systems using synchrotron-radiation techniques. *Trends Anal. Chem.* 29, 528–537 (2010).
- Alam, M. T. et al. Understanding complex electrochemical impedance spectroscopy in corrosion systems using in-situ synchrotron radiation grazing incidence X-ray diffraction. *Electroanglysis* 28, 2166–2170 (2016).
- Ye, Y. et al. Using soft x-ray absorption spectroscopy to characterize electrode/ electrolyte interfaces in-situ and operando. J. Electron Spectrosc. Relat. Phenom. 221 2–9 (2017)
- Davenport, A. J. et al. In situ studies of passive film chemistry using X-ray absorption spectroscopy. Corros. Sci. 35, 19–25 (1993).
- Frankel, G. S. et al. X-ray absorption study of electrochemically grown oxide films on AlCr sputtered alloys; II: in situ studies. J. Electrochem. Soc. 141, 83–90 (1994).
- Davenport, A. J. et al. In situ multielement XANES study of formation and reduction of the oxide film on stainless steel. J. Electrochem. Soc. 141, L6–L8 (1994).
- Davenport, A. J. High resolution in situ XANES investigation og the nature of the passive film on iron in a pH 8.4 borate buffer. J. Electrochem. Soc. 142, 725–730 (1995).
- Schmuki, P. et al. Transpassive dissolution of Cr and sputter-deposited Cr oxides studied by in situ X-ray near-edge spectroscopy. *J. Electrochem. Soc.* 143, 3997–4005 (1996).
- Virtanen, S. et al. Dissolution of thin iron oxide films used as models for iron passive films studied by in situ X-ray absorption near-edge spectroscopy. J. Electrochem. Soc. 144, 198–204 (1997).
- Oblonsky, L. J., Ryan, M. P. & Isaacs, H. S. In situ X-ray absorption near edge structure study of the potential dependence of the formation of the passive film on iron in borate buffe. J. Electrochem. Soc. 144, 2398–2404 (1997).
- Hu, Y. et al. In situ X-ray absorption fine structure and optical reflectance studies of electrodeposited nickel hydrous oxide films in alkaline electrolytes. Can. J. Chem. 75, 1721–1729 (1997)
- Schmuki, P. et al. Electrochemical behavior of Cr2O3/Fe2O3 artificial passive films studied by in situ XANES. J. Electrochem. Soc. 145, 791–801 (1998).
- Oblonsky, L. J., Ryan, M. P. & Isaacs, H. S. In situ determination of the composition of surface films formed on Fe-Cr alloys. *J. Electrochem. Soc.* 145, 1922–1932 (1998).
- Virtanen, S. et al. Electrochemical behavior of Fe in phosphate solutions studied by in situ x-ray absorption near edge structure. *J. Electrochem. Soc.* 146, 4087–4094 (1999).
- Oblonsky, L. J. & Ryan, M. P. In situ x-ray absorption near-edge structure study of the active and transpassive dissolution of passive films on Ni and Ni-Cr alloys in 0.1 M H2SO4. J. Electrochem. Soc. 148, B405–B411 (2001).
- Virtanen, S., Schmuki, P. & Isaacs, H. S. In situ X-ray absorption near edge structure studies of mechanisms of passivity. *Electrochim. Acta* 47, 3117–3125 (2002).
- Le Bozec, N. et al. The role of chromate conversion coating in the filiform corrosion of coated aluminum alloys. J. Electrochem. Soc. 150, B561–B566 (2003).
- De Marco, R. et al. An in situ synchrotron radiation grazing incidence X-ray diffraction study of carbon dioxide corrosion. J. Electrochem. Soc. 152, B389–B392 (2005).
- Leyssens, K. et al. Simultaneous in situ time resolved SR-XRD and corrosion potential analyses to monitor the corrosion on copper. *Electrochem. Commun.* 7, 1265–1270 (2005).

- De Marco, R. et al. An in situ electrochemical impedance spectroscopy/synchrotron radiation grazing incidence X-ray diffraction study of the influence of acetate on the carbon dioxide corrosion of mild steel. *Electrochim. Acta* 52, 3746–3750 (2007).
- Ingham, B. et al. In situ synchrotron X-ray diffraction study of scale formation during CO2 corrosion of carbon steel in sodium and magnesium chloride solutions. Corros. Sci. 56, 96–104 (2012).
- Monnier, J. et al. XAS and XRD in situ characterisation of reduction and reoxidation processes of iron corrosion products involved in atmospheric corrosion. Corros. Sci. 78, 293–303 (2014).
- Watanabe, M. et al. In situ X-ray diffraction measurement method for investigating the oxides films on austenitic stainless steel in simulated pressurized water reactor primary water. Corrosion 71, 1224–1236 (2015).
- Kim, D. H. et al. Oxidation kinetics in iron and stainless steel: an in situ X-ray reflectivity study. J. Phys. Chem. B 108, 20213–20218 (2004).
- Medway, S. L. et al. In situ studies of the oxidation of nickel electrodes in alkaline solution. J. Electroanal. Chem. 587, 172–181 (2006).
- Bertram, F. et al. In situ anodization of aluminum surfaces studied by x-ray reflectivity and electrochemical impedance spectroscopy. J. Appl. Phys. 116, 1–6 (2014).
- Evertsson, J. et al. The thickness of native oxides on aluminum alloys and single crystals. Appl. Surf. Sci. 349, 826–832 (2015).
- Zhang, F. et al. Integration of electrochemical and synchrotron-based X-ray techniques for in-situ investigation of aluminum anodization. *Electrochim. Acta* 241, 299–308 (2017).
- 81. Macdonald, D. D. On the tenuous nature of passivity and its role in the isolation of HLNW. *J. Nucl. Mater.* **379**, 24–32 (2008).
- 82. Macdonald, D. D. The history of the point defect model for the passive state: a brief review of film growth aspects. *Electrochim. Acta* **56**, 1761–1772 (2011).
- 83. Seyeux, A., Maurice, V. & Marcus, P. Oxide film growth kinetics on metals and alloys. *J. Electrochem. Soc.* **160**, C189–C196 (2013).
- Örnek, C. et al. In-situ synchrotron GIXRD study of passive film evolution on duplex stainless steel in corrosive environment. Corros. Sci. 141, 18–21 (2018).
- Aoki, S. et al. Potential dependence of preferential dissolution behavior of a duplex stainless steel in simulated solution inside crevice. Zairyo to Kankyo/. Corros. Eng. 60, 363–367 (2011).
- 86. Olsson, C.-O. A. et al. Quantifying the metal nickel enrichment on stainless steel. *Electrochem. Solid State Lett.* **14**, C1–C3 (2011).
- Fredriksson, W. et al. Full depth profile of passive films on 316L stainless steel based on high resolution HAXPES in combination with ARXPS. Appl. Surf. Sci. 258, 5790–5797 (2012).
- 88. Bearden, J. A. X-ray wavelengths. Rev. Mod. Phys. 39, 78-124 (1967).



Open Access This article is licensed under a Creative Commons Attribution 4.0 International License, which permits use, sharing,

adaptation, distribution and reproduction in any medium or format, as long as you give appropriate credit to the original author(s) and the source, provide a link to the Creative Commons license, and indicate if changes were made. The images or other third party material in this article are included in the article's Creative Commons license, unless indicated otherwise in a credit line to the material. If material is not included in the article's Creative Commons license and your intended use is not permitted by statutory regulation or exceeds the permitted use, you will need to obtain permission directly from the copyright holder. To view a copy of this license, visit http://creativecommons.org/licenses/by/4.0/.

© The Author(s) 2019